

Dual-Polarity GRAPPA for simultaneous reconstruction and ghost correction of EPI data

W. Scott Hoge¹, Jonathan R. Polimeni²

(1) Department of Radiology, Brigham and Women's Hospital and Harvard Medical School, Boston, MA.

(2) Athinoula A. Martinos Center for Biomedical Imaging, Department of Radiology, Harvard Medical School, Massachusetts General Hospital, Charlestown, MA

Address correspondence to: shoge@bwh.harvard.edu

Purpose: We seek improved image quality from accelerated EPI data, particularly at ultra-high field. Certain artifacts in EPI reconstructions can be attributed to nonlinear phase differences between data acquired using frequency encoding gradients of alternating polarity. These errors appear near regions of local susceptibility gradients, and typically cannot be corrected with conventional Nyquist ghost correction (NGC) methods.

Methods: We propose a new reconstruction method that integrates ghost correction into the parallel imaging data recovery process. This is achieved through a pair of GRAPPA kernels that operate directly on the measured EPI data. The proposed Dual-Polarity GRAPPA (DPG) method estimates missing k-space data while simultaneously correcting inherent EPI phase errors.

Results: Simulation results demonstrate that standard NGC is incapable of correcting higher-order phase errors, whereas the Dual-Polarity GRAPPA kernel approach successfully removes these errors. The presence of higher-order phase errors near regions of local susceptibility gradients is demonstrated with *in vivo* data. DPG reconstructions of *in vivo* 3T and 7T EPI data acquired near these regions show a marked improvement over conventional methods.

Conclusion: This new parallel imaging method for reconstructing accelerated EPI data shows better resilience to inherent EPI phase errors, resulting in higher image quality in regions where higher-order EPI phase errors commonly occur.

Key words: Nyquist Ghost Correction, Parallel Imaging, fMRI, Artifact Correction, Oblique ghosts, GESTE

INTRODUCTION

Echo planar imaging (EPI) is often the sequence of choice for modern fast MR imaging applications. EPI is widely used in functional, diffusion, and perfusion MR imaging of the brain. However, EPI commonly suffers from inherent acquisition artifacts including Nyquist ghosting and geometric distortion.

EPI employs fast gradient switching to rapidly sample k-space, sampling on both positive and negative polarity readout gradients during data acquisition. Gradient hardware imperfections and eddy currents often induce differences between the opposing polarity readout gradient sampling grids. These differences manifest as Nyquist (or N/2) ghosts in the image domain. Most Nyquist ghost correction (NGC) algorithms model the difference between positive and negative readout gradient k-space lines as a first-order (linear-plus-scalar) phase correction offset along the frequency encoding (x) direction in hybrid (x - k_y) space. However, the combined impact of eddy currents, magnetic susceptibility effects, and local spatial sensitivity of multi-channel detectors can potentially introduce higher-order

effects, particularly with dense coil arrays (1), (2). The severity of these artifacts increases with field strength, with pronounced artifacts seen at ultra-high field (≥ 7 Tesla) in tissue regions near air-tissue interfaces, particularly above the paranasal sinuses and ear canals.

Concurrently, geometric distortion artifacts in EPI reconstructions arise from local magnetic field inhomogeneity, which is also more pronounced at ultra-high field strengths. These distortions can be reduced by shortening the EPI echo train. Accelerated parallel imaging (pMRI) methods are often employed for this purpose (3), (4). pMRI methods are model-based, however, and pMRI image quality can degrade when the underlying model differs significantly from the imaging system. With accelerated EPI, the reconstruction model must include EPI phase error correction prior to pMRI reconstruction.

To successfully reconstruct highly accelerated EPI data, three important aspects must be maintained. First, echo spacing must be consistent between the calibration and acquisition data to ensure consistent geometric distortion (5), (6). This can be achieved by employing segmented EPI for the calibration data, with the number of segments equal to the acceleration factor. Second, ghost-free calibration data are required to prevent ghosts in the calibration data from appearing in the reconstructed images. Finally, NGC must be consistent across the accelerated and calibration data (7). This last requirement is difficult to guarantee with current methods, however.

Ghost elimination via spatial and temporal encoding (GESTE) (8) is a method that employs generalized autocalibrating partially parallel acquisitions (GRAPPA) (9) for NGC in unaccelerated single-shot EPI data. In GESTE, each EPI data frame is separated into two subframes: one containing k-space data acquired using positive readout gradients (RO^+) and one containing k-space data acquired using negative readout gradients (RO^-). This results in two subframes undersampled by a factor of 2. Because each subframe was acquired on a single readout polarity, there is no phase modulation between odd and even lines to cause Nyquist ghosting. Missing lines within each undersampled subframe can be restored using GRAPPA. Coherently combining the subframes produces the final ghost-free image. GESTE provides EPI ghost suppression comparable with phase labeling for additional coordinate encoding (PLACE) (10) while maintaining the temporal resolution of the original acquisition. GESTE can reconstruct accelerated EPI data, however the effective undersampling factor of each subframe will be twice the native acquisition acceleration factor, which limits GESTE to relatively low acceleration rates.

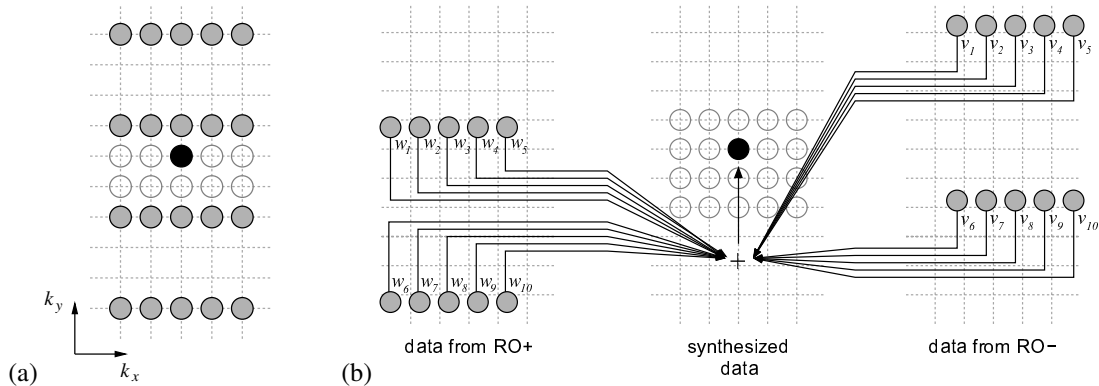


Figure 1. Conventional GRAPPA and the proposed DPG for a kernel of size $N_x = 5$ and $N_y = 4$. (a) Conventional GRAPPA reconstruction model, in which acquired k-space lines from a single frame are used to estimate missing samples. The underlying grid depicts the desired k-space sampling grid. (b) Proposed Dual-Polarity GRAPPA reconstruction model, in which data taken from two distinct frames of EPI data are combined to cancel phase errors while estimating missing samples. The intrinsic phase errors in EPI are depicted by offsets in both k_x and k_y between the acquired sample locations and the desired sampling grid. Gray dots represent source points; black dots represent target points. For simplicity, the coil dimension is not shown.

To specifically address this limitation, we propose embedding the ghost correction process into the GRAPPA reconstruction and including EPI phase correction directly within the pMRI data recovery. This is achieved through a *Dual-Polarity GRAPPA* (DPG) kernel that draws separately from unprocessed RO⁺ and RO⁻ EPI data to synthesize a ghost-free, fully-sampled image. We note that the process of calculating the DPG kernel weights also differs from conventional GRAPPA kernel training, which we describe in the Theory section below.

A secondary benefit is that the DPG kernel provides automatic correction of higher-order EPI phase errors—beyond the simple scalar and linear correction along the frequency encoding direction provided by most NGC methods. Phase errors in EPI data that produce Nyquist ghosts are typically modeled simply as a linear shift between the RO⁺ and RO⁻ sampling grids in the k_x direction. Higher-order errors have been previously considered, e.g. (11), (12), but they are typically difficult to characterize and accurately model *a priori*. The DPG kernel introduced here employs multiple degrees of freedom along both k_x and k_y , and thus efficiently corrects high-order and two-dimensional (2D) phase error terms.

DPG provides the most dramatic improvement in image quality in regions near local field inhomogeneities. We demonstrate herein that EPI phase errors in these regions are markedly non-linear, particularly at ultra-high fields. We further demonstrate that our dual-polarity reconstruction kernel approach accurately compensates for these phase errors with improved EPI image quality.

THEORY

GRAPPA (9), (13) can be described analytically as generating a target point in k-space, \hat{k} , from a weighted linear combination of source points

$$\hat{k} = ck, \quad [1]$$

where c represents the GRAPPA reconstruction weights, k represents the source data, and \hat{k} represents the estimated k-space data. This model is illustrated in Fig. 1(a). The GRAPPA

weights, c , are determined from auto calibration signals (ACS) that are Nyquist sampled. Missing data are then synthesized in subsequent under-sampled MRI acquisitions using the weights, c .

In this study, we employed a *Dual-Polarity GRAPPA* kernel wherein one half of the weights drew from RO⁺ EPI source data and the other half drew from RO⁻ EPI source data. This change requires a dual-kernel analytic model,

$$\hat{k} = wk_+ + vk_-, \quad [2]$$

which is illustrated in Fig. 1(b). We emphasize that $\{k_+, k_-\}$ are EPI data *prior to ghost correction*. This is emphasized in Fig. 1(b), where the EPI k-space data sampled on RO⁺ and RO⁻ are shown shifted from the desired sampling grid. The correction imparted by the DPG kernel corrects these shifts and aligns the k-space data onto the desired sampling grid.

The DPG reconstruction weights are determined in a manner similar to GRAPPA. This requires three frames of calibration data, however: RO⁺ data; RO⁻ data; and derived ghost-free hybrid target data. To identify the DPG parameters, we formed a linear system, $Ax = b$. Similar to GRAPPA, elements of A were drawn from RO⁺ and RO⁻ ACS data, and elements of b from the target data. Solving this system determined DPG reconstruction parameters in the vector, x . The analysis and synthesis process for the DPG kernel is shown in Fig. 2, which illustrates two important differences with conventional GRAPPA. First, DPG image reconstruction requires multiple kernels, each matched to local patterns of RO⁺ and RO⁻ data samples. Second, DPG reconstruction performs EPI phase error correction by generating data estimates at *every k-space location*—for both unacquired k-space lines as in conventional GRAPPA, and for measured k-space data locations. Note that in conventional NGC, measured k-space data are similarly synthesized in a preprocessing step prior to the estimation of missing data via pMRI methods such as GRAPPA.

In conventionally accelerated EPI, ACS data are acquired as segmented EPI with the number of segments equal to the acceleration factor R . This ensures consistent echo spacing, and thus

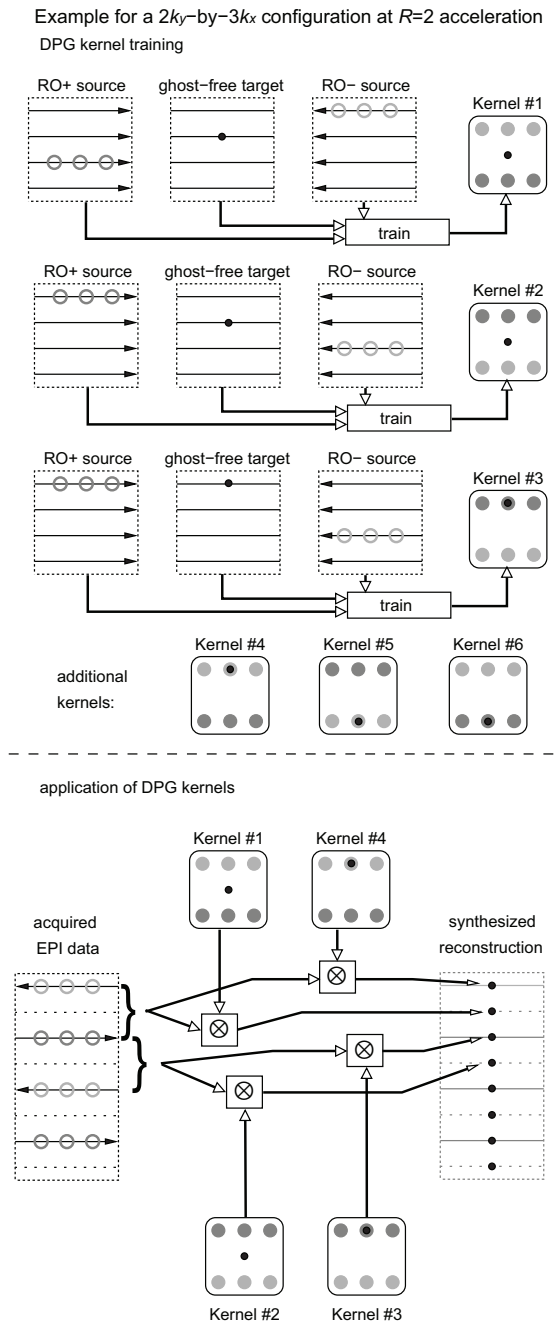


Figure 2. Analysis and synthesis signal flow diagrams for the Dual-Polarity GRAPPA algorithm for $R = 2$ data. On the analysis/training side, three fully-sampled data sets $\{RO^+, RO^-, \text{target}\}$ are used to calibrate each DPG kernel. The six possible DPG kernels for an $R = 2$ configuration are shown, with shaded circles indicating source and target points. The shading corresponds to RO^+ data (dark gray), RO^- data (light gray), and target data (black). On the synthesis/application side, four kernels are chosen to reconstruct the accelerated k-space data. The kernels shown match particular patterns of RO^+ and RO^- samples within the acquired accelerated EPI data. Note that each line of reconstructed k-space is synthesized by at least one of the DPG kernels. Further, some kernels are redundant, in that one may be able to synthesize certain lines of k-space using more than one kernel. Thus, for $R = 2$, only four kernels are needed out of the six possible kernels.

matching geometric distortion, between the ACS and accelerated data (5). To generate the RO^+ , RO^- , and hybrid ACS data sets needed for DPG calibration, we acquired a set of temporally encoded prescan data. For each acquired ACS segment, a second frame of the same data was acquired using readout gradients of opposite polarity. The ACS data were then sorted to form two images consisting entirely of samples from RO^+ lines or from RO^- lines. Ghost-free target calibration data were then formed according to the method summarized in the Appendix. Temporally encoded ACS training data requires twice the acquisition time of a conventional ACS acquisition. Thus, the time needed for DPG calibration ACS data is $(2 \cdot R \cdot TR)$ —i.e., ~ 10 – 20 s for typical EPI protocols.

METHODS

In the experiments below, MR data were acquired from both phantoms and normal, healthy volunteers that were approved by our Institutional Review Board. *In vivo* brain data and anthropomorphic head phantom data were acquired at 7T using an accelerated EPI sequence. For testing, additional water phantom and *in vivo* brain data were acquired at 3T. Temporally encoded ACS data were acquired using a custom segmented fast low-angle excitation echo-planar technique (FLEET)-GESTE (6) prescan, with the total number of segments equal to twice the acceleration factor R . To generate ghost-free target data, the ACS data were sorted and processed as described in the Appendix. After training multiple DPG kernels, fully sampled images were generated from accelerated data by applying the appropriate DPG kernels to the measured EPI data.

For comparison, we reconstructed accelerated EPI data using a state-of-the-art NGC approach based on the local phase correction (LPC) method of Feiweier (2). This method uses three navigator signals acquired immediately prior to the EPI readout, consisting of a single $k_y = 0$ readout line with alternating readout polarities. The first and third navigator lines, corresponding to RO^- , were first averaged and then compared with the second (RO^+) navigator. This method was applied to both the EPI-based ACS data and the accelerated EPI data to correct the shift between the RO^+ and RO^- k-space lines. The LPC parameters were calculated independently for each acquired EPI shot, including each ACS segment and each frame of accelerated EPI data. Conventional GRAPPA parameters were calculated from the LPC-processed ACS data, and were then applied to the LPC-processed accelerated EPI data to synthesize missing k-space data. This method provided conventional images (hereafter referred to as LPC-GRAPPA) to compare against DPG-generated images.

All 7T data were acquired on a Siemens 7T whole-body scanner (Siemens Healthcare, Erlangen, Germany) equipped with SC72 body gradients and a custom-made 32-channel brain array receive coil and a birdcage transmit coil (14). All images were reconstructed using MATLAB (The Mathworks, Natick, MA) on a 64-bit Linux machine, with functions provided by the NC-IGT Fast Imaging Library (15). Coil images were combined using root-sum-of-squares to form the final image.

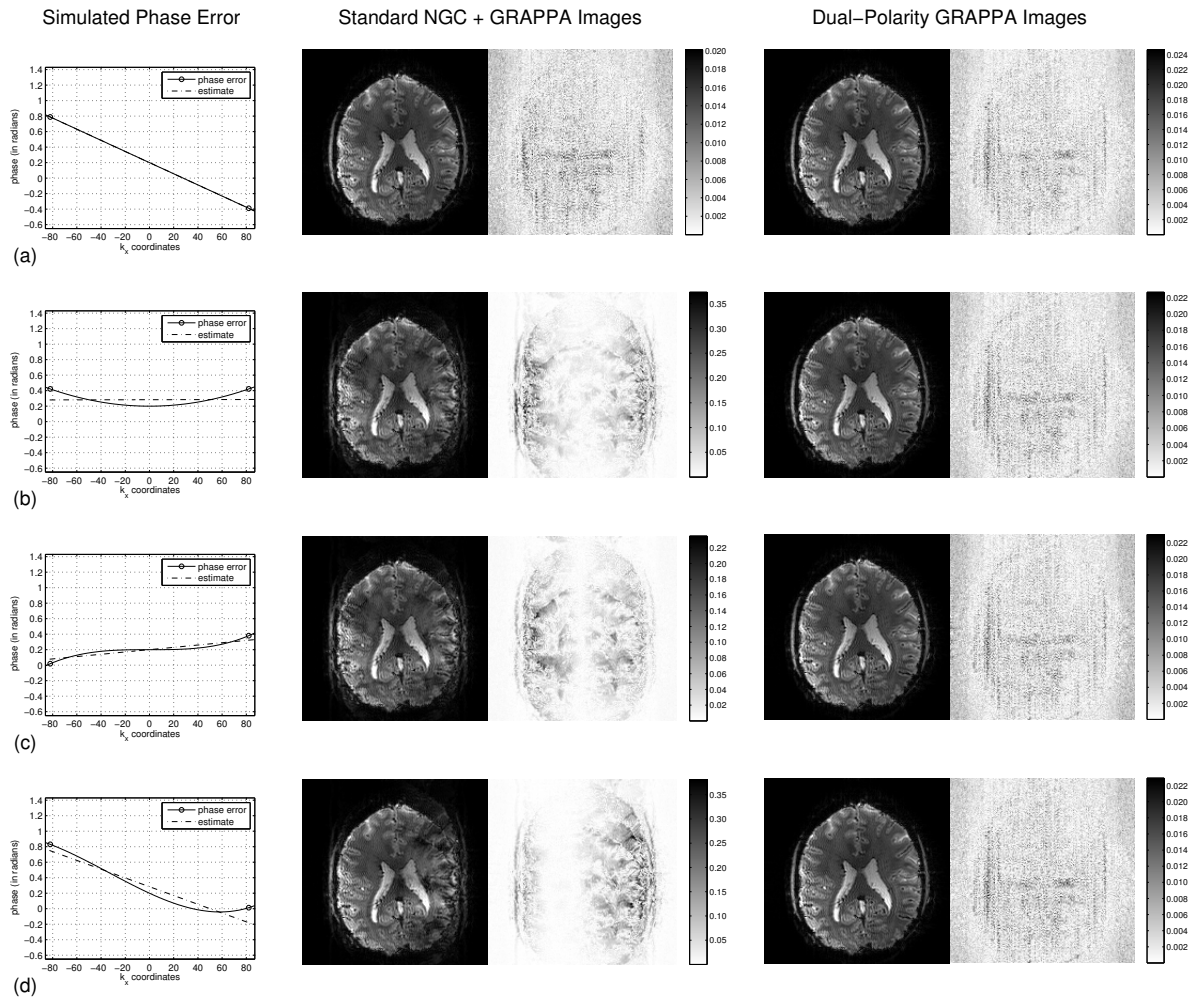


Figure 3. Results from the phase error simulation. Each row shows the simulated phase error introduced to the data (left), and the corresponding reconstructed image and image error for both LPC+GRAPPA (middle) and Dual-Polarity GRAPPA (right). The phase errors were: (a) a constant plus linear; (b) a constant plus quadratic; and (c) a constant plus cubic, respectively. The last row, (d), shows the result of simulating all phase errors (constant plus 1st, 2nd, and 3rd order) simultaneously.

Simulation of higher-order phase error effects

To demonstrate the ability of DPG to accurately model and correct high-order EPI phase errors, we generated synthetic RO⁺ and RO⁻ data from one slice of a ghost-free target data set. Four separate errors were tested: (1) a constant and linear phase error; (2) a constant and quadratic phase error; (3) a constant and cubic phase error; and (4) a linear combination of these three phase errors. These are shown graphically in the left column of Fig. 3. The phase error was applied in the x - k_y hybrid domain, according to the function

$$\bar{k}[x, k_y, c] = k[x, k_y, c] \exp \{j2\pi a_p (x/N_x)^p\}, \quad [3]$$

where a_p is the coefficient for phase error of order p . In the simulation, the phase error coefficient values were set to $\{a_0, a_1, a_2, a_3\} = \{0.2, -1.25, -1.0, 1.2\}$.

Conventional GRAPPA weights were calibrated from the ghost-free data. DGP weights were calibrated from the ghost-free, RO⁺, and RO⁻ data. A $2k_y$ -by- $5k_x$ kernel size was used for both conventional GRAPPA and DPG. An $R = 4$ accelerated acquisition was simulated by drawing k -space lines from

the RO⁺ and RO⁻ data. For the conventional GRAPPA reconstructions, NGC was performed by estimating the linear and constant phase error terms from the phase error function via LPC. These estimated terms were then applied to the synthetic accelerated data to correct the (simulated) phase error, and GRAPPA weights were applied to synthesize missing k -space lines. For DPG, the weights determined in the calibration stage were applied directly to the synthetic accelerated data to generate a full set of synthesized k -space data. For both sets, the final reconstructed image was formed using an IFFT of each coil image, and coil images were combined using root-sum-of-squares.

Data acquired from the anthropomorphic head phantom

Data from an anthropomorphic head phantom were acquired at 7T. The phantom consisted of a plastic shell with an air cavity at the approximate paranasal sinuses location, an outer cavity representing extra-cranial head muscle, and an inner cavity in the geometry of a human brain, with the latter two cavities filled with agarose gel similar to (16). This setup successfully mimics the large, local susceptibility gradient present in the human head.

Unaccelerated ($R = 1$) and accelerated ($R = 4$) data of this phantom were acquired using our single-shot EPI sequence with the following acquisition parameters. The $R = 1$ acquisition employed a nominal $2.0 \times 2.0 \text{ mm}^2$ in-plane voxel size, TE/TR/BW/matrix/flip=36 ms/2890 ms/1776 Hz/pix/96 \times 96/75 $^\circ$, no partial-Fourier, 96 reference lines, FOV=192 cm 2 , with 37 interleaved 1.0-mm thick axial slices (no gap). The accelerated acquisition employed a nominal $1.1 \times 1.1 \text{ mm}^2$ in-plane voxel size, TE/TR/BW/matrix/flip = 26 ms/2000 ms/1512 Hz/pix/174 \times 174/75 $^\circ$, no partial-Fourier, a nominal echo-spacing of 0.79 ms, $R = 4$ acceleration, 128 reference lines, 34 interleaved 1.1-mm thick axial slices (no gap). DPG and GRAPPA both employed a $2k_y$ -by- $5k_x$ kernel.

Additional data were acquired to test the sensitivity of DPG to differences in contrast between the ACS and acquired data. A full description of this experiment is provided in the Supporting Information.
In vivo data acquisition, including regions with strong local magnetic susceptibility gradients

7T data were acquired using two high-resolution, accelerated single-shot gradient-echo EPI protocols: one with nominal $1.5 \times 1.5 \text{ mm}^2$ in-plane voxel size, TE/TR/BW/matrix/flip = 25 ms/2000 ms/1776 Hz/pix/128 \times 128/75 $^\circ$, no partial-Fourier, a nominal echo-spacing of 0.67 ms, $R = 3$ acceleration, 126 reference lines, 37 interleaved 1.5-mm thick axial slices (no gap); and one with nominal $1.1 \times 1.1 \text{ mm}^2$ in-plane voxel size, TE/TR/BW/matrix/flip = 26 ms/2000 ms/1512 Hz/pix/174 \times 174/75 $^\circ$, no partial-Fourier, a nominal echo-spacing of 0.79 ms, $R = 4$ acceleration, 128 reference lines, 34 interleaved 1.1-mm thick axial slices (no gap). For both protocols, 4 dummy measurements were included immediately prior to the accelerated image series to allow the longitudinal magnetization to achieve steady-state. FLEET-GESTE ACS data were acquired using a constant flip angle of 10 $^\circ$ and 5 RF preparation pulses.

Time-series SNR (tSNR) is the principle metric for measuring functional sensitivity without respect to any one specific experiment (4). tSNR quantifies the ability to detect subtle time-series data features in the presence of noise, and can be used to evaluate EPI temporal stability. To assess the sensitivity of LPC+GRAPPA and DPG reconstructed images, we calculated tSNR maps using existing definitions (17). First, rigid-body motion correction was performed with the AFNI (<http://afni.nimh.nih.gov/>) command `3dvolreg` (18), (19) using the middle time-point as a reference. tSNR maps were then generated from the motion-corrected data by dividing the temporal standard deviation by the temporal mean after linear detrending.

In vivo data to demonstrate the sensitivity to DPG kernel size

For the DPG kernel to accurately capture and model shift between RO $^+$ and RO $^-$, the distance between the two sampling coordinate grids must be smaller than the width of the DPG kernel along k_x . This is demonstrated through the use of *in vivo* brain data acquired from a healthy normal subject. The data were acquired on a Siemens 3T Trio system, using a custom EPI sequence that allowed one to deliberately induce

large shifts along k_x . The EPI acquisition parameters were TR/TE/flip/FOV/matrix=1.12 s/27 ms/78 $^\circ$ /24 cm 2 /64 \times 64 with 21 slices, acceleration factor $R = 2$, and a standard 12-channel head coil. A single slice from the 21 acquired slices is shown. The gradient timing was adjusted to produce a k_x coordinate shift of $\sim 11 \Delta k_x$ samples. Three shift correction strategies were tested: a small $2k_y$ -by- $5k_x$ DPG kernel; a large $2k_x$ -by- $13k_y$ DPG kernel; and a two-stage correction using LPC correction first to remove the large linear shift, followed by a small $2k_y$ -by- $5k_x$ DPG kernel.

Phantom data to demonstrate DPG in the presence of 2D phase errors

Phase errors can be found along k_y when the three physical gradients G_x , G_y , and G_z , that produce the readout gradient waveform do not generate identical eddy current-induced delays or do not have identical gradient amplifier responses. This leads to a phase shift in each k_y line that alternates in polarity between RO $^+$ and RO $^-$ gradients (20), (21), (22). This alternating phase offset leads to a “bunching” of the k_y lines (22), as depicted in Fig. 1(b), which manifests as Nyquist ghosting. This “oblique ghost” is often more pronounced during oblique slice prescriptions, when multiple gradient coils are recruited to form the encoding gradients. Oblique ghosts require 2D phase correction (20), (22), because conventional NGC methods only correct phase errors along k_x .

To demonstrate that DPG can remove alternating phase errors along the phase encoding direction, k_y , and thus remove oblique ghosts, we acquired phantom data with a double-oblique slice orientation. EPI data were acquired from a spherical water phantom on a 3T GE EXCITE scanner and a standard 8-channel-receiver head coil. The nominal $3.33 \text{ mm} \times 3.33 \text{ mm} \times 6 \text{ mm}$ resolution protocol parameters were: TR/TE/BW/flip/FOV/matrix = 800 ms / 31.6 ms / 2500 Hz/pix / 80 $^\circ$ / 32 cm 2 / 96 \times 96 with ten 5 mm thick slices (1 mm gap) and no acceleration ($R = 1$).

GESTE can remove 2D phase errors arising from oblique EPI acquisitions (8). One therefore expects that DPG calibration target data will be similarly ghost-free, even in the presence of phase errors along k_y . Because the severity of oblique ghosts is dependent on eddy current compensation performance and may not be present on all MRI systems, we first confirmed the presence of 2D phase errors by calculating a 2D phase map from the RO $^+$ and RO $^-$ images as described by Chen & Wyrwicz (20). We then confirmed that the DPG reconstruction was capable of correctly compensating for these errors.

RESULTS

Simulation of high-order phase errors along k_x

Our simulated phase error experiments (Fig. 3) demonstrate that DPG is capable of estimating and correcting non-linear phase errors. Plots in the leftmost column show each synthetic phase error function used to generate synthetic RO $^+$ and RO $^-$ data. The dashed line shows the LPC linear fit, which yields constant and linear parameters for phase error correction before GRAPPA reconstruction.

Each row of Fig. 3 shows a comparison between the current standard reconstruction approach versus DPG. Because phase errors were synthesized, the reconstruction error for each image is

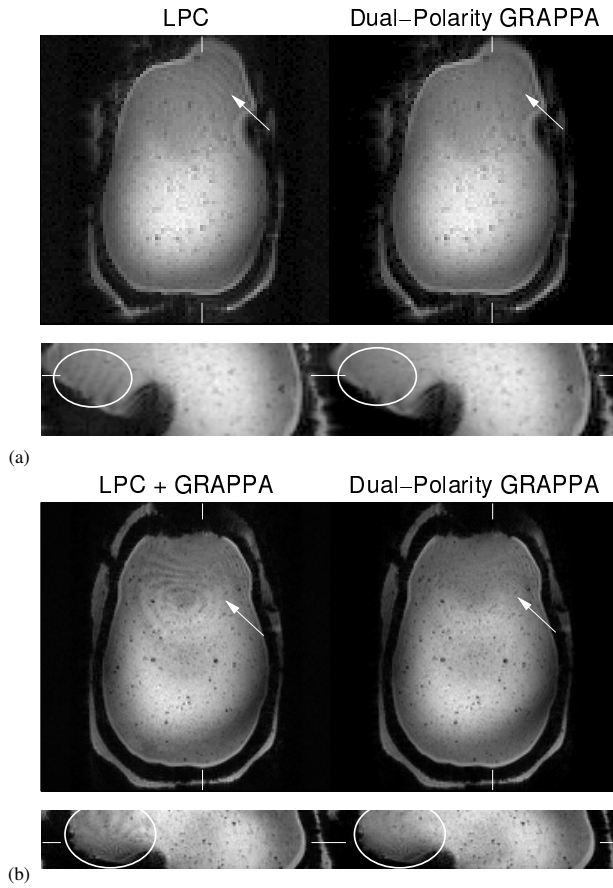


Figure 4. Images from an anthropomorphic head phantom, showing the ability of DPG to remove the interference pattern artifact in both (a) unaccelerated (i.e., $R = 1$) and (b) $R = 4$ data.

available and shown to the right of each image. Because the standard approach models the phase error using only a constant and linear term, the conventional GRAPPA images associated with higher-order phase errors show significant artifacts. Only the central regions of each GRAPPA image (corresponding to the regions where the phase difference is linear) show low error. In contrast, DPG provides high-quality reconstructions for each of the simulated phase error functions.

We note that one could modify the standard NGC approach to model higher-order phase errors as well. However, these models would need to be explicitly stated for each EPI acquisition scenario. Adding additional model terms in scenarios where they are not needed may lead to over-fitting, which could reduce image quality. Secondly, standard phase error correction methods are typically employ only 3–5 lines of navigator data. Performing a high-order fit to such limited, and possibly noisy, data is prone to estimation error as well. In contrast, DPG automatically provides a suitable mechanism to capture and correct higher-order phase error terms, without requiring an explicit phase error model.

Head phantom results

Although the DPG method was developed primarily for reconstructing accelerated EPI data, it can also provide ghost cor-

rection for unaccelerated, $R = 1$, data. Fig. 4(a) shows a comparison between the LPC method and DPG for unaccelerated 7T head phantom data. Susceptibility-induced geometric distortion is seen in the upper-right region of the image. Near this large geometric distortion, a phase interference “ripple” pattern is apparent. In the reformatted sagittal view, the LPC images show ripples present in multiple slices near the air/gel interface region. Notably, these ripples are predominantly absent from the DPG images, which show a much more inform intensity profile over the corresponding regions in both the axial and sagittal views.

Fig. 4(b) shows images from $R = 4$ accelerated head phantom data. Although geometric distortion is reduced (due to the reduced effective echo spacing), phase interference artifacts are again visible in the LPC+GRAPPA reconstructions. The sagittal images demonstrate that these artifacts extend far above the region of local field inhomogeneity. Again, these artifacts are substantially reduced in the DPG reconstructions.

Additional images reconstructed from accelerated anthropomorphic head phantom data demonstrating the resilience of DPG to image contrast and spatial resolution differences between the ACS data and the measured accelerated data are presented in Supporting Fig. S1.

Results from *in vivo* data in regions of susceptibility gradients

Fig. 5 illustrates examples of higher-order EPI phase errors *in vivo*. Phase differences are seen between the RO^+ and RO^- navigator signals for one set of $R = 3$ 7T EPI data. The phase maps highlight the readout direction phase difference in hybrid $(x-k_y)$ space, across multiple coils and slices. The signal for a particular coil and slice is highlighted in the lower right panel. Although phase differences along the readout in hybrid $(x-k_y)$ space are commonly modeled as linear, we have found that there often exist significant non-linear components near regions of local field inhomogeneity. While this non-linearity appears to be associated with local magnetic field variations, they are not seen in every coil channel which is likely due to differences in the reception fields for each detector. For example, a given coil sensitivity may be low in the region of the local magnetic field variation. While these non-linearities are not found in every slice or coil, they occur often enough to be problematic for conventional NGC methods. Non-linearity in the navigator phase difference can bias the NGC parameter estimation, which leads to model mismatch between the acquired and pMRI calibration data, causing phase interference “ripple” patterns.

Images from four different subjects acquired at $R = 3$ and $R = 4$ are shown in Fig. 6. Note that the NGC navigator data from Fig. 5 correspond to the image data in Fig. 6(a), while the axial slice shown corresponds to slice 12 referred to in Fig. 5(c). Each panel highlights a comparison between the LPC+GRAPPA and DPG reconstructions for slices acquired just above either the paranasal sinuses or the ear canal—locations well known for local magnetic field inhomogeneity. In each comparison, arrows highlight regions that exhibit phase interference ripple artifacts in the LPC+GRAPPA images (left). In contrast, the DPG reconstructions (right) show improved compensation of the high-order phase errors with images of significantly higher quality. Images

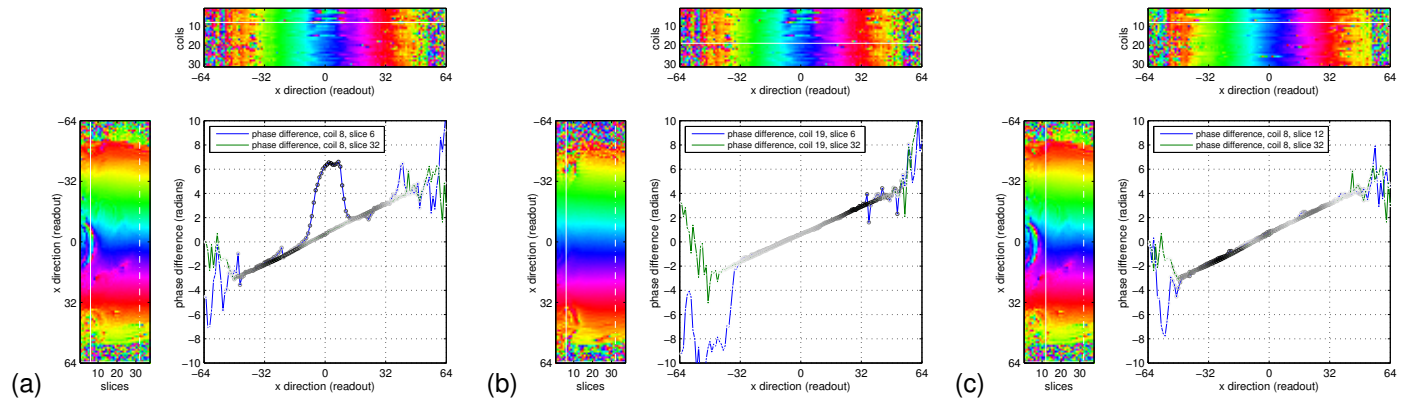


Figure 5. Phase differences between standard RO^+ and RO^- navigator lines used in conventional NGC methods, shown in the hybrid $x-k_y$ domain and displayed across all coil channels and image slices. The line plot in each panel shows the phase differences for a single coil channel in two slices: (a) coil channel 8 in slices 6 and 32, (b) coil channel 19 in slices 6 and 32, and (c) coil channel 8 in slices 12 and 32. (The axial image corresponding to slice 12 of this dataset is also shown in Fig. 6(a).) Lower slice numbers correspond to more inferior slice locations. Non-linear phase differences are evident in many coils within the inferior slice locations, which are proximal to the region of B_0 inhomogeneity. The intensity of the circles in the line plot correspond to the magnitude of the navigator signal, with higher intensity represented by darker circles—the navigator signal magnitude is used as a weighting term in the LPC method to de-emphasize locations in hybrid space where the navigator signal is less reliable on account of the low sensitivity of the coil.

from the reformatted sagittal view are also shown, with white dashes indicating the relative location of each axial slice. In addition, the interference pattern region is highlighted with a white ellipse. These regions show that the interference pattern artifact extends over a large region. In each case, the use of DPG yields images with significantly reduced artifacts and higher fidelity to the underlying anatomy than LPC+GRAPPA.

To assess the impact of ripple artifacts on the sensitivity of functional, diffusion, or perfusion imaging sensitivity, the tSNR measured from one representative $R = 3$ data set is shown in Fig. 7, for both the LPC+GRAPPA and DPG reconstructions. It is notable that even though all k -space lines are synthesized in DPG, DPG produces equal or higher tSNR across all slices. A close-up of a local magnetic field inhomogeneity region is provided in Fig. 7(c). Here, the tSNR in the vicinity of the interference pattern artifact highlighted previously is low in the LPC+GRAPPA reconstruction compared to the DPG reconstruction.

Fig. 7(d) directly compares the time-series standard deviation (i.e., the denominator of the tSNR) of the LPC+GRAPPA and DPG reconstructions, as a ratio of $\sigma_{LPC}/\sigma_{DPG}$. This image demonstrates that the lower tSNR in the LPC+GRAPPA images is due to increased temporal variance, and not simply lower image intensity levels. The ratio will be higher at locations where the DPG image reconstruction yields lower variance throughout the time series compared to LPC+GRAPPA. Indeed, $\sigma_{LPC}/\sigma_{DPG}$ is markedly higher in regions of the ripple artifact. Together, these results indicate that DPG both removes the high-order phase error interference pattern ripple artifact, and maintains better tSNR and temporal stability in regions of the brain near local magnetic susceptibility. One can expect that this will provide improved sensitivity for EPI-based applications.

Sensitivity to DPG kernel size and complementarity of DPG with conventional phase correction methods

As stated previously, the shift between RO^+ and RO^- must be smaller than the kernel extent along k_x for DPG to be successful. Fig. 8 illustrates data with a large shift between RO^+ and RO^- , and how LPC and DPG can be combined to mitigate this need. Fig. 8(a-c) shows DPG calibration data from one coil in k -space. The dashed horizontal lines illustrate the relative distance in k -space between the RO^+ and RO^- echo centers. The shift in each set measures approximately $\sim 5.65 \Delta k_x$ sample points away from the target $k_x = 0$ location.

Fig. 8(d-f) shows images reconstructed using the DPG method with: a small kernel size; a large kernel size; and a small kernel size after first applying LPC, respectively. The small-kernel reconstruction in Fig. 8(d) shows a significant deterioration in image quality because the width of the kernel is much smaller than the shift between RO^+ and RO^- along k_x . The second scenario, Fig. 8(e), demonstrates that image quality can be recovered if the DPG kernel is large enough to cover the entire k_x shift. However, the disadvantage here is two-fold: knowledge of the linear shift is needed *a priori*; and large DPG kernels require much greater computational and memory costs. Fig. 8(f) demonstrates that a small DPG kernel size can be used if the large gross shift is removed first. This scenario demonstrates that LPC and DPG are complementary, with LPC employed to first perform a linear correction of gross misalignment along k_x , followed by DPG to correct residual high-order phase errors.

Demonstration of effectiveness correcting 2D phase errors

Fig. 9 demonstrates the effectiveness of DPG in the presence of 2D phase errors. The phase difference between the RO^+ and RO^- calibration data—after removing the linear phase difference along x —is shown in Fig. 9(a). This double-oblique data shows a strong phase error along the y direction, indicating the presence of 2D phase offsets between the RO^+ and RO^-

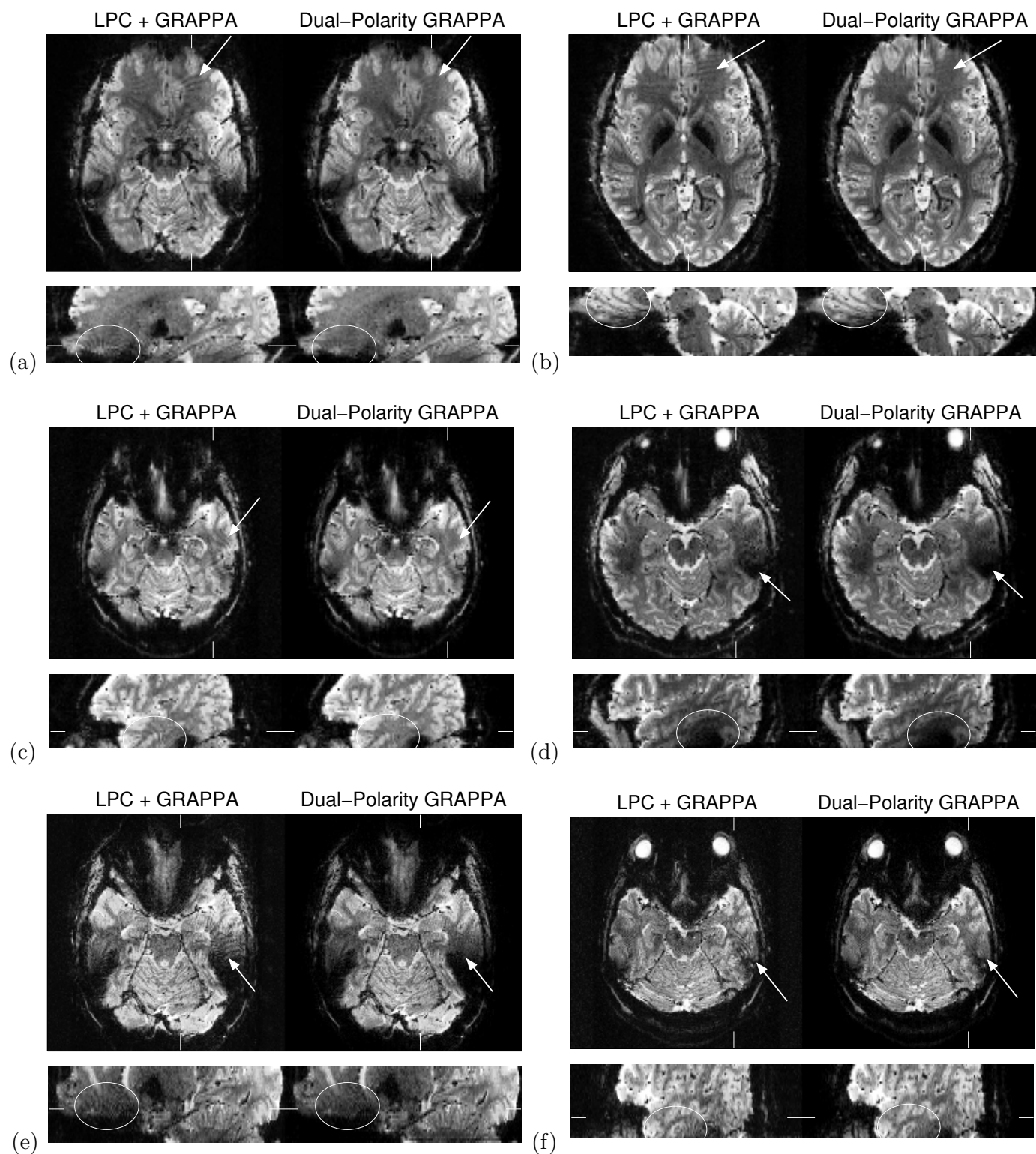


Figure 6. Comparisons between conventional LPC+GRAPPA and DPG reconstructions, focused on images near regions with local susceptibility gradients. Four 7T subjects (a–d) with $R = 3$ acceleration and two additional 7T subjects (e–f) with $R = 4$ acceleration are shown. White dashes show the relative location of the alternate image. Interference pattern artifacts are highlighted with arrows in the axial images, and by the white ellipse in the sagittal views.

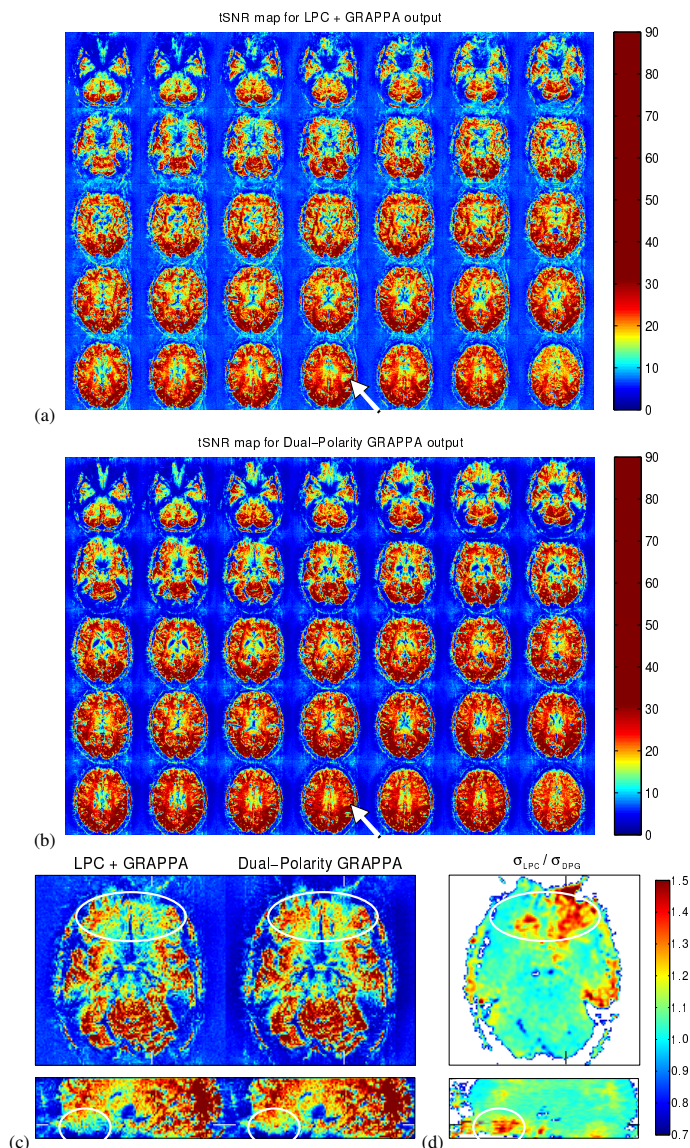


Figure 7. Comparison of tSNR maps for the $R = 3$ 7T data set shown in Fig. 6(a), windowed to emphasize the lower-third of the dynamic range. (a) tSNR for 35 slices reconstructed by the LPC+GRAPPA method; (b) tSNR for the same data reconstructed using DPG. Arrows indicate example focal regions where tSNR is notably higher with DPG than in the LPC+GRAPPA reconstruction, both above the paranasal sinuses and a region near the ear canals. (c) A highlight of one axial and one sagittal-reformatted slice emphasizing regions (indicated by ellipses) with interference pattern artifacts. (d) An image of the ratio between the LPC+GRAPPA and DPG temporal signal variance, highlighting regions where DPG outperforms LPC+GRAPPA in terms of tSNR.

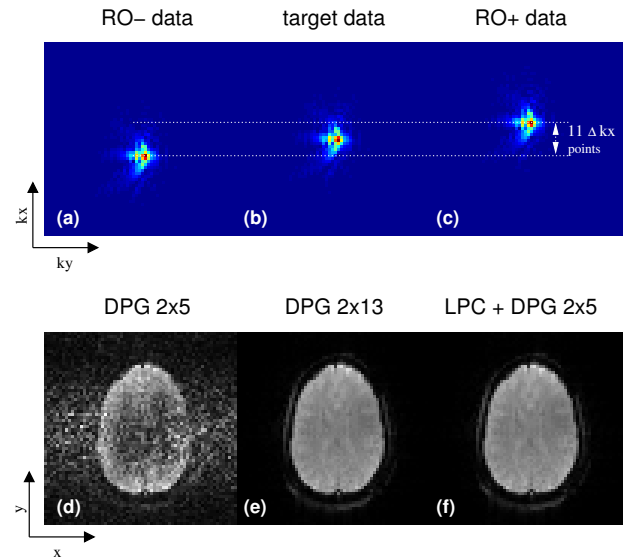


Figure 8. Results from the experiment to demonstrate DPG sensitivity to kernel size and integrating conventional phase correction into the DPG reconstruction as a preprocessing step. (a–c) DPG k -space calibration data for one coil, demonstrating a case with a large coordinate shift along k_x between RO^+ and RO^- . (d–f) Image reconstructions from three different scenarios: (d) a small DPG kernel; (e) LPC combined with the small kernel; and (f) a large DPG kernel. The images demonstrate LPC and DPG are compatible—LPC can be used to first estimate the linear component and correct the large shift, while DPG can be used afterward to mitigate higher-order phase error effects.

lines. The image reconstructions of the unaccelerated data are shown in Fig. 9(b). The images reconstructed with the conventional LPC+GRAPPA method exhibit a clear oblique ghost artifact consistent with the phase variation shown in Fig. 9(a). This oblique ghost is eliminated in the DPG reconstruction, demonstrating that the DPG kernel is capable of removing Nyquist ghosts arising from errors along the both the k_x and k_y directions.

DISCUSSION

Our *in vivo* results show that the conventional model of linear-plus-constant phase error between RO^+ and RO^- EPI signals is often violated, particularly at ultra-high field strength and certain receive coil configurations. The simulation and *in vivo* data demonstrate that even small errors in the phase correction coefficient estimation can produce significant phase interference artifacts reconstructed images. Although the LPC method allows fitting higher-order/nonlinear basis functions to the phase difference between RO^+ and RO^- which may help reduce these artifacts (2), appropriate basis sets are difficult to determine *a priori*. Furthermore, selecting an appropriate basis set may be complicated by a dependence on the particular coil geometry as well as the body region being imaged.

With its ability to automatically estimate higher-order phase errors, we find that DPG reconstructions yield higher quality images than conventional phase-error correction and pMRI techniques currently provide. The ability of the DPG method to re-

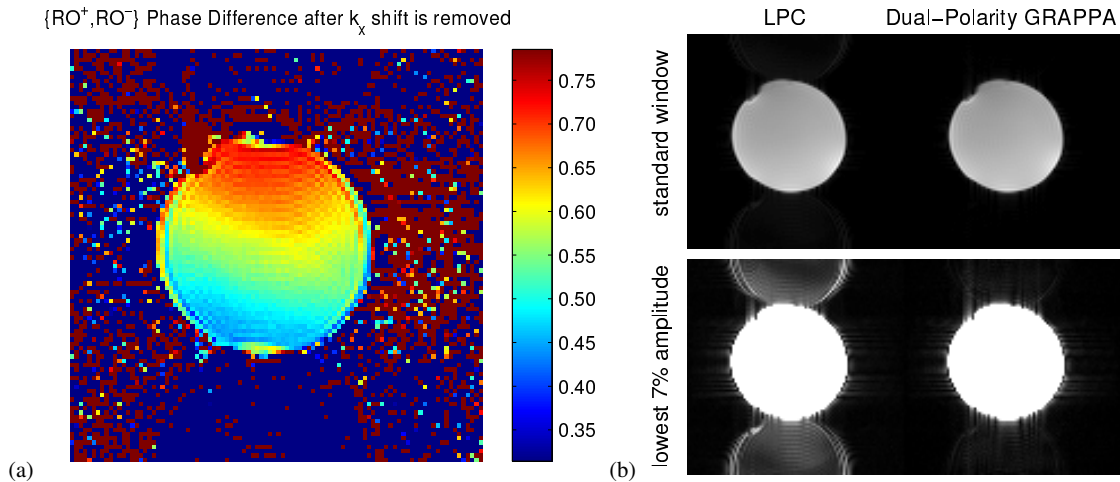


Figure 9. A demonstration of the DPG method correcting oblique EPI ghosts caused by 2D phase errors. (a) A 2D phase error map (in radians) calculated as the phase difference between the RO^+ and RO^- frames of the GESTE ACS data. A phase difference trend is seen in the vertical phase encoding (y) direction, indicating the presence of alternating phase errors between odd and even k_y lines. (b) Image reconstructions of the corresponding unaccelerated ($R = 1$) data. The top row presents images with typical windowing. The bottom row presents the same images with windowing adjusted to better visualize ghost regions. The LPC+GRAPPA reconstruction shows an oblique ghost, which is properly corrected in the DPG reconstruction.

move rapidly varying higher-order phase errors may depend on the DPG kernel size, however—a potential relationship currently under investigation.

One notable difference between conventional GRAPPA and Dual-Polarity GRAPPA is that DPG synthesizes all k -space lines. In sequences other than EPI, this is considered to be detrimental as the SNR improves if original data are retained (23), (24). In EPI, however, the original data likely contain phase errors. These errors are ostensibly corrected by standard NGC methods, but these corrections are often insufficient in the presence of 2D or higher-order phase errors. Although it may at first appear counter-intuitive to not include the original sampled data in the final output, using DPG to synthesize all k -space lines enables the correction of high-order phase errors and better image quality with the same or better tSNR.

DPG has an additional advantage in that it removes many implementation ambiguities. DPG removes the need to explicitly model higher-order phase error terms—which may or may not be present. It also removes the possibility of NGC estimation error by eliminating the need for navigator signals. Further, in conventional LPC+GRAPPA, ghost correction is applied twice: once for calibration data, and once for accelerated data. If either correction is insufficient, the pMRI reconstruction will degrade. In contrast, DPG ensures consistent ghost correction across the calibration and reconstruction data. This may be one reason why the tSNR of the DPG reconstructed data is often better than images formed from the standard approach.

One potential disadvantage of DPG is the dependence on pre-scan data. Modern EPI applications acquire a series of image repetitions. Current standard practice is to employ pre-scan data to calculate pMRI reconstruction weights, so DPG and conventional GRAPPA are consistent in this regard. Furthermore, the additional time required for DPG to acquire temporally encoded ACS data is often negligible. Nonetheless, even slight motion during a long functional scan can alter the coil loading, which

can potentially induce complex phase changes in the received signal. The resilience of DPG in the presence of motion and the development of a motion robust version of the DPG algorithm constitute an active area of research.

CONCLUSIONS

We have presented a method to reconstruct images from sub-sampled multi-channel EPI data by embedding the ghost correction step within the pMRI reconstruction process. This approach provides three key advantages: (1) the use of pre-scan data removes the possibility of biased ghost correction parameters derived from the EPI NGC navigator lines from adversely impacting the pMRI reconstruction step; (2) model consistency between the pMRI calibration and reconstruction stages is maintained; and (3) the DPG kernel comprises coefficients extending in both k_x and k_y , which enable DPG to successfully mitigate 2D and high-order EPI phase errors. Together, these advantages provide improved image quality compared with current state-of-the-art EPI reconstruction methods.

ACKNOWLEDGMENTS

Support for this work was provided in part by the Functional Neuroimaging Laboratory at the Brigham and Women's Hospital, NIH NIBIB K01-EB011498 and R01 EB019437 (Polimeni), and by the Athinoula A. Martinos Center for Biomedical Imaging. We also thank Dr. Bastien Guérin for use of his anthropomorphic head phantom, and Drs. Keith Heberlein and Kavin Setsompop for valuable discussions.

REFERENCES

1. Keil B, Wald LL. Massively parallel MRI detector arrays. *Journal of Magnetic Resonance* 2013;229:75–89.
2. Feiweier T. Magnetic resonance method and apparatus to determine phase correction parameters, 2013. US Patent 8,497,681.

3. de Zwart JA, van Gelderen P, Golay X, Ikonomidou VN, Duyn JH. Accelerated parallel imaging for functional imaging of the human. *NMR in Biomedicine* 2006;19(3):342–351.
4. Wald LL, Polimeni JR. High-speed, high-resolution acquisitions. in *Brain Mapping: An Encyclopedic Reference* (Toga AW, ed.). San Diego, CA.: Academic Press, 2015; .
5. Skare S, Newbould RD, Clayton DB, Albers GW, Nagle S, Bammer R. Clinical multishot DW-EPI through parallel imaging with considerations of susceptibility, motion, and noise. *Magn Reson Med* 2007;57(5):881–890.
6. Polimeni JR, Bhat H, Witzel T, Benner T, Feiweier T, Inati SJ, Renvall V, Heberlein K, Wald LL. Reducing sensitivity losses due to respiration and motion in accelerated Echo Planar Imaging by reordering the autocalibration data acquisition. *Magn Reson Med* 2015;Earlyview. In press (DOI: 10.1002/mrm.25628).
7. Polimeni JR, Setsompop K, Hoge WS. Characterization of autocalibration methods for accelerated EPI reconstructions using GRAPPA. in *Proc Joint Annual ISMRM-ESMRMB Scientific Meeting*. 2014; 4397.
8. Hoge WS, Tan H, Kraft RA. Robust EPI Nyquist ghost elimination via spatial and temporal encoding. *Magn Reson Med* 2010;64(6):1781–1791.
9. Griswold MA, Jakob PM, Heidemann RM, Nittka M, Jellus V, Wang J, Kiefer B, Haase A. Generalized autocalibrating partially parallel acquisitions (GRAPPA). *Magn Reson Med* 2002;47(6):1202–1210.
10. Xiang QS, Ye FQ. Correction for geometric distortion and N/2 ghosting in EPI by phase labeling for additional coordinate encoding (PLACE). *Magn Reson Med* 2007;57(4):731–741.
11. Buonocore MH, Zhu DC. Image-based ghost correction for interleaved EPI. *Magn Reson Med* 2001;45(1):96–108.
12. Chen NK, Avram AV, Song AW. Two-dimensional phase cycled reconstruction for inherent correction of echo-planar imaging Nyquist artifacts. *Magnetic Resonance in Medicine* 2011;66(4):1057–1066.
13. Wang Z, Wang J, Detre J. Improved data reconstruction method for GRAPPA. *Magn Reson Med* 2005;54(3):738–42.
14. Keil B, Triantafyllou C, Hamm M, Wald LL. Design optimization of a 32-channel head coil at 7T. in *Proc Intl Soc Mag Reson Med*. 2010; 18:1493.
15. National Center for Image Guided Therapy. Fast imaging library. <http://www.spl.harvard.edu/publications/item/view/1393>.
16. Graedel NN, Polimeni JR, Guérin B, Gagoski B, Wald LL. An anatomically realistic temperature phantom for radiofrequency heating measurements. *Magnetic Resonance in Medicine* 2015;73(1):442–450.
17. Triantafyllou C, Polimeni JR, Wald LL. Physiological noise and signal-to-noise ratio in fMRI with multi-channel array coils. *Neuroimage* 2011; 55(2):597–606.
18. Cox RW. AFNI: software for analysis and visualization of functional magnetic resonance neuroimages. *Comput Biomed Res* 1996;29(3):162–73.
19. Cox RW, Jesmanowicz A. Real-time 3D image registration for functional MRI. *Magn Reson Med* 1999;42(6):1014–8.
20. Chen NK, Wyrwicz AM. Removal of EPI Nyquist ghost artifacts with two-dimensional phase correction. *Magn Reson Med* 2004;51:1247–1253.
21. Zhou X, Maier J, Epstein F. Reduction of Nyquist ghost artifacts in oblique echo planar imaging. US Patent 5,672,969, 1997.
22. Xu D, King KF, Zur Y, Hinks RS. Robust 2D phase correction for echo planar imaging under a tight field-of-view. *Magn Reson Med* 2010; 64(6):1800–1813.
23. Wang J, Kluge T, Nittka M, Jellus V, Kühn B, Kiefer B. Parallel acquisition techniques with modified SENSE reconstructions: mSENSE. in *Proc of First Wurzburg Workshop*. 2001; 92.
24. Preibisch C, Wallenhorst T, Heidemann R, Zanella FE, Lanfermann H. Comparison of parallel acquisition techniques generalized autocalibrating partially parallel acquisitions (GRAPPA) and modified sensitivity encoding (mSENSE) in functional MRI (fMRI) at 3t. *J Magn Reson Imaging* 2008;27(3):590–598.
25. Bhat H, Polimeni JR, Cauley SF, Setsompop K, Wald LL, Heberlein K. Motion insensitive ACS acquisition method for in-plane and simultaneous multi-slice accelerated EPI. in *Proc Joint Annual ISMRM-ESMRMB Scientific Meeting*. 2014; 644.
26. Hoge WS, Tan H, Kraft RA, Polimeni JR. Improved ghost-correction in multi-shot EPI using PLACE and GESTE. in *Proc Joint Annual ISMRM-ESMRMB Scientific Meeting*. 2014; 1638.

APPENDIX

The image quality of pMRI reconstruction methods depend greatly on accurate calibration data. In this work, we employ EPI-based calibration data. Thus, reconstructed image quality will be improved if the calibration data is ghost-free. Towards

this end, we employ GESTE (8) to generate ghost-free target data for DPG calibration. The original GESTE study focused on single-shot EPI data. Here, we extend the method to multi-shot EPI data.

GESTE requires temporally-encoded data. For multi-shot EPI, we reverse the readout gradient polarity for each segment and acquire multiple shots for each slice before proceeding to the next slice, as in FLEET (6), (25). FLEET reduces artifacts from dynamic effects such as respiration and other motion between interleaves, while GESTE removes static artifacts that arise from eddy current and constant magnetic susceptibility effects.

Fig. 10 illustrates the full signal flow of our approach to generate ACS data from multi-shot EPI. For the RO^+ and RO^- calibration data, we reorder the temporally-encoded multi-shot data, correcting constant phase differences between the shots as needed. For the ghost-free target data, the processing occurs in two passes. First, the ACS data is corrected using LPC (2) to align each data segment readout onto the same sampling grid. The readouts are then reordered to form the RO^+ and RO^- data sets, each sampled at the Nyquist-rate. The data are then averaged to form bootstrap calibration data and a *temporary* set of GRAPPA coefficients, c . We note that the bootstrap method here differs slightly from our original method (26), where the first pass was performed without any navigator signals. We have since found that using phase correction navigators gives better DPG performance.

In the second stage, the original multi-shot data is paired segment-wise and coherently combined to cancel phase errors present in each segment pair. Then, each composite segment is reconstructed using the temporary GRAPPA weights c . This produces a complete Nyquist-rate image for each segment pair. These images are then coherently combined to form the final ghost-free target data.

To illustrate typical artifact and noise levels present at each stage in the process, images from multiple points in the signal flow are shown in the center column of Fig. 10.

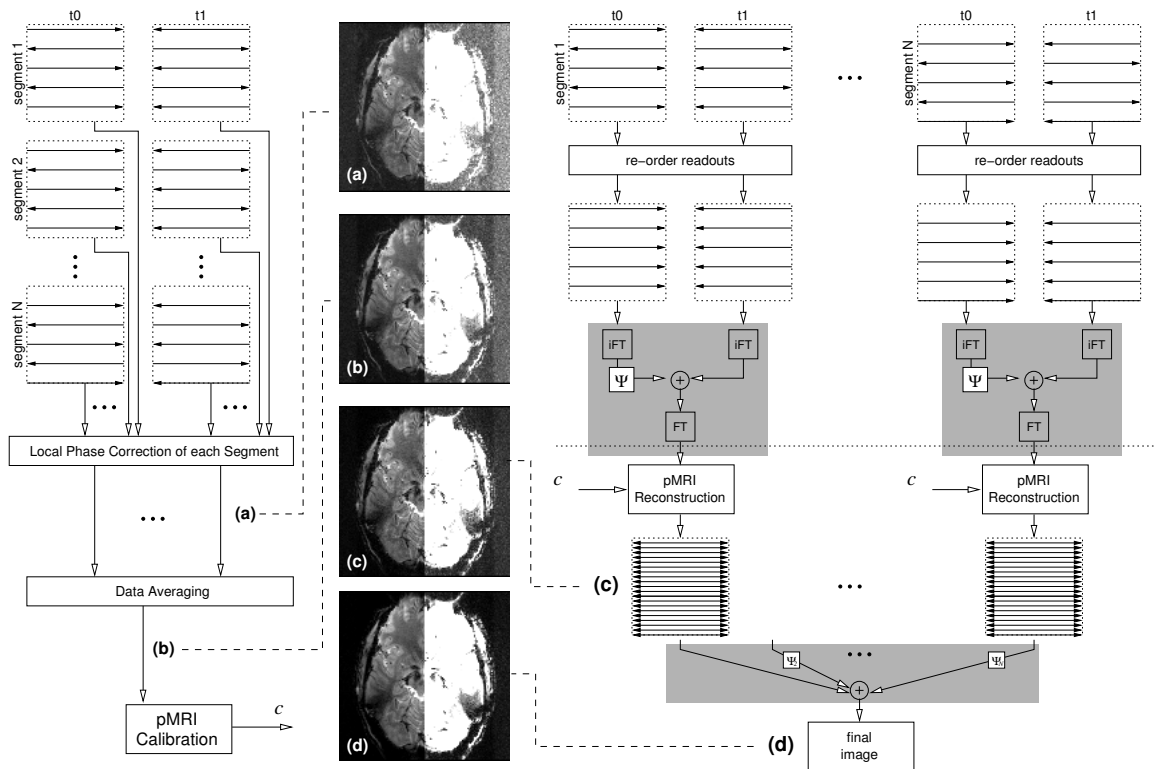


Figure 10. Signal flow diagram for GESTE processing of multi-shot EPI calibration data. In the first stage (left), all of the segments are phase corrected and averaged, in order to generate *temporary* GRAPPA coefficients, c . In the second stage (top right), each of the segments are ghost-corrected using PLACE. In the third stage (bottom right), GESTE is used to combine the PLACE-corrected segments and generate the target calibration data. Example images at various points in each stage are shown in (a–d), with the left half showing typical windowing, and the right half showing the lowest 10% of the image signal.

SIMULATION TO DEMONSTRATE THAT SMALL IMAGE FEATURES ARE RETAINED WITH DPG

Supporting Methods

Data from an anthropomorphic head phantom with an air cavity approximately at the anatomical location of the frontal sinuses was acquired using the accelerated EPI sequence at 7T. The phantom consists of a plastic shell with an outer cavity representing extra-cranial head muscle and an inner cavity in the geometry of a human brain, both filled with agarose gel similar to that in (1).

The volume of gel within the anthropomorphic head phantom contains multiple air bubbles, which we use here to simulate the appearance of small lesions in human anatomy. To calibrate DPG reconstruction parameters from “lesion free” images, we filtered the original calibration data using a 3×3 median filter template. Magnitude and phase signals were blurred separately, and the phase signal was unwrapped to ensure the median filter was operating on numerically similar data within its template. The 2D phase unwrapping step employed the branch cuts method based on phase residues, described by Ghiglia & Pritt (2). The blurred version of the phantom ACS data were then used to generate DPG coefficients. These were then applied to unprocessed 1.5 mm^3 -isotropic $R = 3$ accelerated EPI phantom data [TE/TR/BW/matrix/flip = 25 ms/2000 ms/1776 Hz/pix/128 \times 128/75°, no partial-Fourier, a nominal echo-spacing of 0.67 ms, 126 reference lines, 37 interleaved 1.5-mm thick axial slices (no gap)]. The accelerated data were reconstructed using three approaches: the LPC+GRAPPA and DPG methods using the original ACS data; and DPG using the spatially-filtered ACS data.

Supporting Results

Images from the anthropomorphic head phantom data to demonstrate the resilience of DPG to differences in contrast between the ACS data and measured accelerated data are shown in Fig. S1. The original ACS data for one coil is shown in Fig. S1(a), with the corresponding blurred images shown in Fig. S1(b). One can notice that the most of the gel bubble features visible in the original ACS data have been effectively eliminated by median filtering. The images in Fig. S1(c) show the data reconstructed using three approaches to determine whether the DPG method is capable of retaining fine details needed for high-resolution studies, even when these fine details are absent from the ACS data. On the left, the image resulting from a standard LPC+GRAPPA reconstruction is shown. The other images show the DPG reconstructions using the original ACS data (center) and the filtered ACS data (right). A portion of the image that highlights a region with both large and small bubbles is shown at the upper left of each sub-image. A visual comparison of these images show that DPG is able to resolve the bubble features with the same resolution as the standard LPC+GRAPPA approach. DPG has the additional advantage that the non-linear phase artifacts visible in the top portion of the LPC+GRAPPA image are absent in the DPG images.

REFERENCES

1. Graedel NN, Polimeni JR, Guérin B, Gagoski B, Wald LL. An anatomically realistic temperature phantom for radiofrequency heating measurements. *Magnetic Resonance in Medicine* 2014;73(1):442–450.
2. Ghiglia DC, Pritt MD. *Two-Dimensional Phase Unwrapping: Theory, Algorithms, and Software*. Wiley-Interscience, 1998.

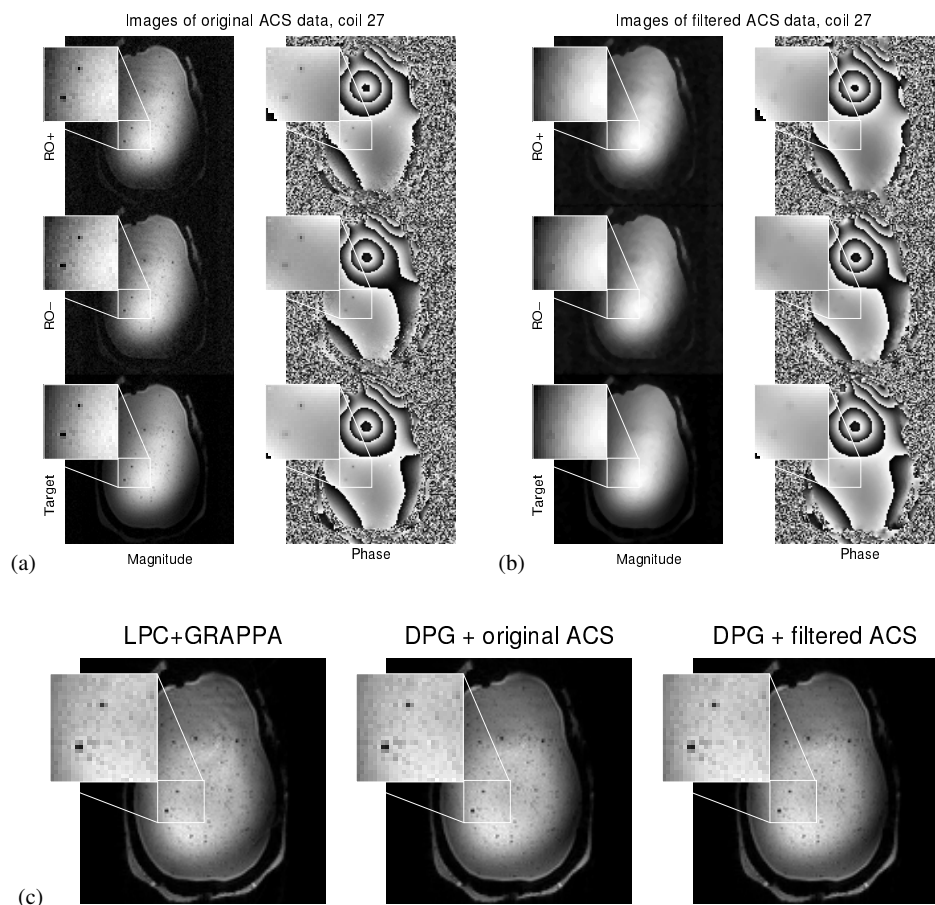


Figure S1. Images from the simulated phantom lesion experiment. (a) Original ACS data from one coil; (b) the corresponding 3×3 median filtered ACS data. (c) Images reconstructed from the $R = 3$ accelerated EPI data. From left to right, the images show: (left) LPC+GRAPPA image using unfiltered ACS data; (middle) a DPG image using kernel parameters calibrated using the unfiltered ACS data in panel (a); (right) a DPG reconstruction using kernel parameters calibrated using the median-filtered ACS data in panel (b). Gel bubbles visible in the highlighted region show comparable resolution across all three methods, indicating that the small image features are maintained in the DPG reconstructions, even when these features are absent from the ACS data.